IEEE Access
Multidisciplinary ⋮ Rapid Review ⋮ Open Access Journal

Received 14 July 2024, accepted 25 July 2024, date of publication 5 August 2024, date of current version 14 August 2024.

Digital Object Identifier 10.1109/ACCESS.2024.3438107

RESEARCH ARTICLE

Diffuse-LOS Optical Wireless Communication Across Wavy Water-Air-Interface Using UVA Light

CHENYU GUO, ZENGXIN LI, LULU ZHA, ZHICHONG WANG, HAOLIN JIA, (Graduate Student Member, IEEE), YUQI HOU, JIANYANG SHI, (Member, IEEE), ZIWEI LI, JUNWEN ZHANG, NAN CHI, (Senior Member, IEEE), AND CHAO SHEN, (Senior Member, IEEE)

Key Laboratory for Information Science of Electromagnetic Waves (MoE), School of Information Science and Technology, Fudan University, Shanghai 200433, China

Corresponding author: Chao Shen (chaoshen@fudan.edu.cn)

This work was supported in part by the Natural Science Foundation of China Project under Grant 62031011, Grant 62274042, and Grant 61925104; and in part by the Key Research and Development Program of Jiangsu Province under Grant BE2021008-5.

ABSTRACT Underwater Wireless Optical Communication (UWOC) holds significant implications in the realms of marine scientific observation, marine military security, and marine resource utilization. Overcoming the challenges associated with cross-medium information transmission represents a pivotal research frontier within the domain of underwater Internet of Things (IoT). This paper investigates the across water-air-interface ultraviolet light uplink communication in the presence of waves. Different degrees of diffuse-line-of-sight and different sizes of waves are studied in the communication link to assess their impact on transmission performance. Using non-return-to-zero on-off keying (NRZ-OOK) modulation, a data transmission of 17.4 Mbit/s is achieved with a lateral displacement of 5 cm in still water, and 17.1 Mbit/s data transmission is achieved under aligned 12 mm wave amplitude condition. A method is proposed to reduce the dependence on relay in across water-air-interface communication when the optical transmitter and receiver are not aligned, and the effectiveness of using ultraviolet light communication under large wave conditions is demonstrated. Bit error rate and received optical power indicate that increasing wave size and deviation of the transceivers both result in channel attenuation in the water-air-interface channel, thus degrading link performance.

INDEX TERMS Wireless optical communication, across water-air-interface communication, ultraviolet light, diffuse-line-of-sight, waves.

I. INTRODUCTION

Given that two-thirds of the Earth's surface is submerged beneath oceans, the marine environment hosts invaluable resources pivotal for fostering sustainable human progress, thereby rendering it strategically imperative for fostering high-caliber development initiatives [1]. Underwater wireless communication (UWC) assumes a central role across commercial, scientific, and military domains, underscoring an acute need for long-distance, high-speed underwater wireless communication technologies [2].

Presently, prominent underwater wireless communication technologies encompass underwater acoustic communication (UAC), radio frequency (RF) communication, and blue-green light communication [3]. UAC holds a decisive advantage in communication range, achieving transmission distances of up to tens of kilometers. However, its available bandwidth is confined to approximately 20 kHz, yielding transmission rates in the order of tens of kilo-bit-per-second (Kbit/s) [4], [5], [6]. RF communication offers elevated rates, scaling to hundreds of Kbit/s; nevertheless, it confronts limitations

The associate editor coordinating the review of this manuscript and approving it for publication was Liam Barry.

TABLE 1. Comparisons among three UWC technologies. [12], [26].

Types	Distance	Frequency	Bandwidth	Data rate	Consumption	Latency	Transmission Power
Acoustics	Several tens of kilometers	10 Hz-1 MHz	kHz	Kbit/s	High	High	Tens of Watts (typical value)
RF	Several tens of meters	30-300 Hz	MHz	Mbit/s	High	Moderate	Few mW to hundreds of Watts (distance dependent)
Optical	Several hundred meters	10^{12}-10^{15} Hz	MHz-GHz	Gbit/s	Low	Low	Few Watts

due to skin effect during underwater transmission, consequently constraining transmission ranges considerably. Consequently, RF communication proves suitable for short-range communication in shallow waters but confronts hurdles in deep-sea scenarios [7].

Researchers have proposed underwater wireless optical communication (UWOC) as an effective solution to address the high power consumption, high latency, inability to simultaneously achieve high data rates and long-distance communication, among other limitations, associated with RF and UAC [8]. UWOC offers an exceptionally high modulation bandwidth, enabling data transmission rates exceeding giga-bit-per-second (Gbit/s) [9]. Additionally, it boasts an effective transmission range of several hundred meters. Moreover, UWOC utilizes non-licensed optical spectra beyond the radio frequency spectrum, thus being considered an efficient solution to circumvent spectrum congestion [10]. Furthermore, compared to UAC and RF, UWOC features lower-cost optical transceivers such as light-emitting diodes (LEDs), laser diodes (LDs), and photodiodes (PDs), offering advantages such as low power consumption and high cost-effectiveness [11], [12]. A comparison of the three UWC technologies is presented in Table 1.

While there has been research on visible light (especially blue-green light) communication systems for high-speed, long-distance transmission across static air-water interfaces, such line-of-sight (LOS) communication systems suffer from the requirement of strict alignment of direct light, rendering them unable to provide stable communication performance in practical scenarios [13]. In the presence of underwater turbulence, LOS communication becomes inefficient due to misalignment between the transmitting and receiving ends caused by variations in the refractive index of the medium [14]. Moreover, due to alignment requirements, direct line-of-sight communication fails to offer extensive communication coverage for mobile users.

In contrast, diffuse-line-of-sight (Diffuse-LOS) communication holds great promise as it can establish effective communication channels even when there is misalignment between the transmitting and receiving ends [15]. This characteristic ensures the feasibility of using diffuse light communication for across water-air interfaces. Although blue-green light is favored in underwater wireless optical communication due to its low attenuation in water, ultraviolet (UV) light presents significant advantages in some complex channels owing to its low background radiation

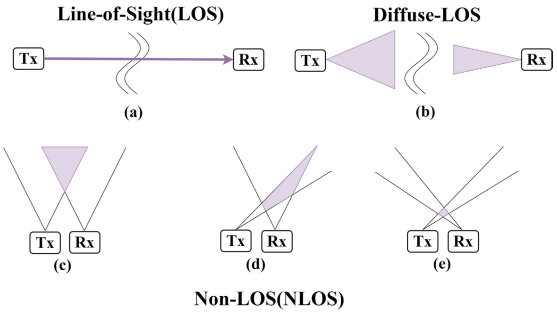

FIGURE 1. (a). Line-of-sight (LOS) link. (b). Diffuse-LOS link. (c,d,e). Non-LOS link.

and equipment noise resulting from absorption by the ozone layer. Moreover, compared to blue-green light, the UV light, through its scattering interactions with free-space particles and solution particles, can effectively establish Diffuse-LOS links or even non-line-of-sight (NLOS) links [3]. The UOWC communication modes of LOS, NLOS, and Diffuse-LOS are illustrated in the Fig. 1.

In real sea waves, stable communication across the air-water interface can be achieved by combining the spatiotemporal characteristics of waves with adaptive methods [30]. We believe that applying this approach to the UV band, along with the scattering properties of UV light, presents a highly attractive research direction.

Furthermore, considering the communication between remotely operated underwater vehicles (ROVs) and unmanned aerial vehicles (UAVs), integrating the advantages of blue-green and UV light communication could be beneficial. As shown in Fig. 2. In scenarios with weak wave conditions or minimal deviation between the transmitter and receiver, blue-green light communication can achieve lower attenuation and better communication quality. Conversely, under strong wave conditions or significant deviations between the transmitter and receiver, UV light communication can provide a more stable communication link. In summary, integrating blue-green and UV light communication and employing different strategies based on varying scenarios is likely to be a key direction for future research.

The performance of UWOC links is closely associated with three main factors: scattering, absorption, and turbulence [12]. Scattering occurs when suspended particles and bubbles in the water cause the light beam to deviate from its initial path, resulting in diffusion. Absorption is the loss

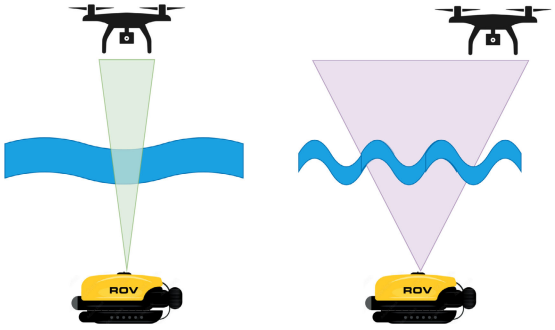

FIGURE 2. Communication strategies between ROV and UAV in two typical scenarios (a). Weak wave, minimal deviation, using blue-green light. (b). Strong wave, severe deviation, using UV light.

of signal in the link due to water molecules, salts, or other particles. Turbulence arises from the uneven refractive index of the water caused by dissolved substances or suspended particles, leading to light path deviation. The attenuation of light in the water varies greatly across different depths due to factors such as variations in phytoplankton density, sunlight intensity, and salinity [16]. Exploring the impact of these factors on underwater channels is crucial in the UWOC field.

However, there is little UWOC research about the wavy effects on diffuse-line-of-sight across water-air-interface [17], [18], [19], especially concerning the utilization of LEDs with wavelengths in the range of 370 nm to 400 nm. In the lab, we innovatively established an uplink channel with 378 nm LED and APD410 across the quartz water tank varied with the misalignment degree and wave size. The mismatch between the transmitter (Tx) and receiver (Rx) exerted a negative impact on the performance of UWOC links owing to the degradation of received signal optical power. Hence, the exploration of UWOC links amidst surface currents and tides gains importance, facilitating the development of a more realistic scenario for UWOC links in marine environments.

II. RELATED RESEARCH

In 2019, Sun et al. achieved high-speed communication at 11 Mbit/s using non-return-to-zero on-off keying (NRZ-OOK) and quadrature amplitude modulation (QAM)-orthogonal frequency division multiplexing (OFDM) modulation techniques, with a transmitter-receiver separation of 5 cm, covering an area of 79 cm^2 [17]. In 2020, Sun et al. established a NLOS link in highly turbid port waters with a data rate of 85 Mbit/s and a transmission distance of 30 cm using ultraviolet laser and photomultiplier tube (PMT) with OOK modulation [20]. In 2021, Cao et al. proposed a single-scattering path loss (PL) model for NLOS-UVC systems based on LEDs, deriving analytical expressions by modeling the LED emission pattern as a Lambertian distribution [21].

Research on across air-water communication using different wavelength light sources as optical transmitters, as well as studies on the impact of various factors leading to changes in the underwater channel on communication performance, are equally worthy of attention. In 2019, Sait et al. investigated the effects of medium inhomogeneity caused by the quantity of bubbles and temperature gradients on 377 nm ultraviolet LD underwater communication [22]. The results indicated that turbulence induced by temperature gradients only caused slight channel fading, while different quantities and sizes of bubbles enhanced received optical power due to capturing ultraviolet scattered light. In 2021, Yu et al. studied the influence of off-axis angles on received signals and the impact of different fields of view (FOV) on communication performance when using 520 nm LD with engineered diffuser (ED) and ground glass diffuser (GGD) [23]. In 2022, Qin et al. utilized Monte Carlo simulations to evaluate the comprehensive effects of surface waves, link length, water turbulence, wave speed, and receiver parameters on communication performance in across air-water downlink channels, validated experimentally using 488 nm LD [19]. Also in 2022, Sahoo and Shanmugam employed Monte Carlo simulations to investigate the impact of bubble rate, receiver aperture, beam width, and divergence angle on data transmission performance, proposing a method to mitigate channel fading caused by bubbles by expanding beam width and reducing beam divergence angle [28]. Table 2 presents summaries of several significant wireless optical communication research achievements about different communication modalities.

III. CHANNEL CHARACTERIZATION

A. UNDERWATER CHANNEL

The interaction between photons and particles in water is frequent and intense. Fig. 3 illustrates the behavior of a light beam encountering particles while propagating through water. When a laser transmits through a water body, part of the light is absorbed by the water, while another part is scattered. To mathematically describe these two effects, two wavelength-dependent optical characteristic parameters—absorption coefficient $a(\lambda)$ and scattering coefficient $b(\lambda)$— are introduced. The attenuation coefficient $c(\lambda)$ can be expressed as follows [31]:

$$c(\lambda) = a(\lambda) + b(\lambda) \tag{1}$$

where λ represents the wavelength of the light, and the ratio of $b(\lambda)$ to $c(\lambda)$ is the albedo.

Furthermore, the transmitted light, denoted as I, can be expressed as follows [32]:

$$I = I_0 e^{-c(\lambda)z} \tag{2}$$

where I_0 is the transmission optical power and z is the propagation distance.

Underwater optical scattering can be classified into Rayleigh scattering by small molecules and Mie scattering by large molecules and suspended particles in the water. Since the radii of the equivalent spherical particles in water are larger than the wavelength of the incident light, the scattering

TABLE 2. Researches of different communication modalities in wireless optical communication system.

Modality	Transmitter	Receiver	Technique	Data Rate	Distance	Reference
LOS	520nm-LD	PIN	OOK	3.4 Gbit/s	1.8 m in water	[24]
LOS	520nm-LD	APD210	OFDM	5.5 Gbit/s	26 m in water	[25]
LOS	RGB-LD	PD	Gaussian to CAFAB conversion	20 Gbit/s	100 m in water	[2]
NLOS	377nm-LD	PMT	OOK	72-85 Mbit/s	30 cm in water	[20]
NLOS	265nm-LED	PMT	OOK, PPM	2.4 Kbit/s	100 m in air	[27]
Diffuse-LOS	365nm-LED	APD430	OOK, OFDM	30.2-111.4 Mbit/s	60 cm in air + 30 cm in water	[17]
Diffuse-LOS	294nm-LED	APD430	OFDM	71 Mbit/s	8 cm in air	[18]
Diffuse-LOS	450nm-LD	APD	DMT	2.5 Gbit/s	5 m in air	[29]
Diffuse-LOS	378nm-LED	APD410	OOK	17.1 Mbit/s, 17.4 Mbit/s	20 cm in air + 10 cm in water	This work

[a]Transmitter: LED stands for light-emitting diode; LD stands for laser diode.
[b]Technique: PPM stands for pulse-position modulation; OOK stands for on-off keying modulation; OFDM stands for orthogonal frequency-division multiplexing modulation; DMT stands for discrete multitone modulation; CAFAB stands for circular auto-focusing Airy beam.
[c]Receiver: PIN stands for PIN photodetector; PMT stands for photomultiplier tube; APD stands for avalanche photodiode detector.

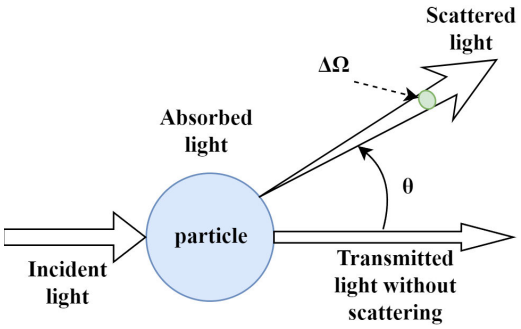

FIGURE 3. Light propagation when encountering a particle in water.

model in seawater can be effectively considered as a Mie scattering model.

According to the Mie scattering theory for spherical particles, it can be derived that [33]:

$$c(\lambda) = \pi \int_{r_1}^{r_2} r^2 Q_{\text{ext}} f(r) \mathrm{d}r \tag{3}$$

where r is the particle radius; $f(r)$ represents the particle radius distribution function, such as a hyperbolic distribution or the commonly used logarithmic distribution for aerosol particles. r_1 and r_2 denote the minimum and maximum particle radii, respectively. $\int_{r_1}^{r_2} f(r)dr$ represents the number of particles per unit volume of water. Q_{ext} is the extinction efficiency factor, depicted as:

$$Q_{\text{ext}} = \frac{\sigma_{\text{ext}}}{\pi r^2} = \frac{2}{\alpha^2} \sum_{n=1}^{\infty} (2n+1)\,\text{Re}\,(a_n + b_n) \tag{4}$$

where σ_{ext} is the extinction cross-section, α is the particle size parameter given by $\alpha = \frac{2\pi r}{\lambda}$, and a_n and b_n are the Mie scattering coefficients.

After light is scattered by seawater, it deviates from its original propagation direction. The spatial intensity distribution of the new propagation direction is referred to as the volume scattering function (VSF), which is defined as:

$$\beta(\theta;\lambda) = \lim_{\Delta r \to 0} \lim_{\Delta\Omega \to 0} \frac{\Phi_s(\theta;\lambda)}{\Phi_i(\lambda)\Delta r \Delta\Omega} \tag{5}$$

where the unit of the volume scattering function β is $\text{m}^{-1}\text{sr}^{-1}$. Δr represents the path length of the medium, $\Delta\Omega$ (Fig. 3) is the solid angle, and $\Phi_s(\theta;\lambda)$ denotes the power of the scattered light within the unit solid angle at the scattering angle θ (Fig. 3). $\Phi_i(\lambda)$ represents the power of the incident light. Therefore, the volume scattering function can be considered as the ratio of the scattered light power per unit length and unit solid angle to the incident power.

By integrating $\beta(\theta;\lambda)$ over the entire solid angle, we obtain:

$$b(\lambda) = \int_{4\pi} \beta(\theta;\lambda)\mathrm{d}\Omega = 2\pi \int_0^{\pi} \beta(\theta;\lambda)\sin\theta d\theta \tag{6}$$

In the above equation, since the distribution of scattering directions should exhibit rotational symmetry about the incident direction, the integration over the entire 4π solid angle can be simplified to the form on the rightmost side.

Dividing the VSF β by the scattering coefficient b yields the scattering phase function (SPF) $\tilde{\beta}$.

$$\tilde{\beta}(\theta;\lambda) = \frac{\beta(\theta;\lambda)}{b(\lambda)} \tag{7}$$

The SPF describes the probability distribution of the new propagation direction after scattering.

Measuring the SPF is highly challenging for several reasons. Firstly, its magnitude varies significantly across different angles, often spanning several orders of magnitude, necessitating instruments with a wide dynamic range. Secondly, the phase function of seawater changes rapidly at very small forward angles, demanding high precision from the instrumentation. Consequently, researchers have developed analytical formulas that approximate the actual phase function. Currently, the most widely used approximation

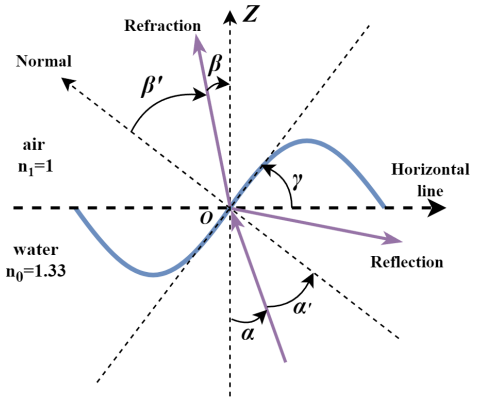

FIGURE 4. A simplified model for light propagation across the water-air interface.

is the Henyey-Greenstein function [34], abbreviated as HG function, defined as follows:

$$\widetilde{\beta}(g;\theta) = \frac{1}{4\pi}\frac{1-g^2}{\left(1+g^2-2g\cos\theta\right)^{3/2}} \tag{8}$$

where g is a factor used to adjust the relative magnitude of forward and backward scattering. A value of g closer to 1 indicates a higher likelihood of forward scattering, while a value closer to -1 indicates a higher likelihood of backward scattering. The HG function is straightforward in form and its inverse can also be computed, making it highly convenient for practical use.

B. WATER-AIR INTERFACE

When light from an LED illuminates the interface between water and the atmosphere, some of the light is reflected back, while another portion is refracted into the air. The passage of light through the sea-air interface model is illustrated as shown in Fig. 4.

The sea surface exhibits a random undulating state. Assuming the refractive index of the atmosphere is n_1 and that of seawater is n_2, as depicted in Fig. 4, establish a Cartesian coordinate system where the xy-plane is parallel to the sea surface. The z-axis is oriented vertically upward from the sea surface at the origin O. The tangent of the wave at O forms an angle γ with the x-axis. Consider an incident light ray inclined at an angle α to the vertical line, corresponding to an incident angle $\alpha' = \gamma - \alpha$. The refracted light beam forms an angle β with the zenith direction, and the refracted angle is $\beta' = \gamma - \beta$. According to the law of refraction:

$$n_0 \sin\alpha' = n_0 \sin(\gamma-\alpha) = n_1 \sin\beta' = n_1 \sin(\gamma-\beta) \tag{9}$$

$$\beta = \arcsin\left(\frac{n_0}{n_1}\sin(\gamma-\alpha)\right) \tag{10}$$

After passing through the water-air interface, the light beam continues to propagate in a straight line along the refracted direction.

When light travels from an optically denser medium (such as seawater) to an optically rarer medium (such as air), the critical angle for total internal reflection α_c can be calculated using the following formula:

$$\alpha_c = \arcsin\left(\frac{1}{1.33}\right) \approx 0.84\text{rad} \approx 48.59^\circ \tag{11}$$

The refractive index of seawater is approximately 1.33 and remains relatively constant within the visible light wavelength range. In contrast, the refractive index of the atmosphere is approximately 1.0003, significantly lower than that of seawater. Therefore, when light travels from seawater to the atmosphere, if the angle of incidence is less than the critical angle for total internal reflection, approximately 48.6 degrees, the light will transmit through the water surface into the atmosphere. However, if the angle of incidence exceeds the critical angle, greater than approximately 48.6 degrees, the light will be reflected back into the seawater and cannot transmit into the atmosphere. This phenomenon is crucial in visible light inter-medium transmission to ensure that the angle of incidence does not exceed the critical angle, as it would otherwise prevent the transmission of optical signals.

To describe three-dimensional irregular ocean waves, a linear superposition method can be employed. Based on the characteristics of the wave spectrum, maximum and minimum frequencies can be selected, and the frequency range can be divided into n segments. For each frequency segment, the waves can be further divided into m segments based on angles. Within each frequency and angle segment, parameters such as amplitude, frequency, wave number, and initial phase can be calculated. These parameters are then used in the cosine wave expression to obtain the cosine waveforms for each frequency and angle segment. Finally, all cosine waves are linearly superimposed to derive the three-dimensional form of irregular ocean waves. From observed wave data, the wave spectrum $S(\omega)$ and directional function $G(\omega,\theta)$ can be computed, enabling wave inversion. The purpose of inversion is to deduce parameters such as wave amplitude, frequency, wave number, direction, as well as the spatial and temporal distribution of waves based on observational data. The linear superposition method is a commonly used inversion technique, where a set of linear equations is solved to compute various wave parameters. The mathematical description of waves is as follows [36]:

$$\eta(x,y,t) = \sum_{i=1}^{n}\sum_{j=1}^{m} a_{ij}\cos\left[\omega_{ij}t - k_{ij}\left(x\cos\theta_j + y\sin\theta_j\right) + \varepsilon_{ij}\right] \tag{12}$$

In the equation, the wave amplitude is defined as: $a_{ij} = \sqrt{2S\left(\omega_i,\theta_{j\Phi}\right)\Delta\omega\Delta\theta}$, where $\theta_{j\Phi}$ represents the angle between wave direction and wind direction, defined as $\theta_{j\Phi} = -\pi + (j-0.5)\Delta\theta$. The wave direction relative to the x-axis is given by $\theta_j = \Phi - \pi + (j-0.5)\Delta\theta$, where Φ is the direction angle. The intervals between frequencies and angles are defined as $\Delta\omega = (\omega_H - \omega_L)/n$ and $\Delta\theta = 2\pi/m$, respectively. ε_{ij} denotes uniformly distributed random numbers between 0

and 1, introduced to prevent the repeated superposition of identical frequencies. The simplified one-dimensional model of (12) is:

$$\eta(x,t) = a\cos(kx - \omega t + \phi) \tag{13}$$

where η is the surface elevation, a is the wave amplitude, k is the wave number, ω is the angular frequency, and ϕ is the phase.

Each light beam's refraction angle and intensity on various small facets of a simulated sea surface can be calculated using the laws of refraction and geometric optics. By summing the refracted intensities from all rays at different refraction angles, the spatial distribution of total LED visible light refracted intensity on the water-air interface can be determined. However, this approach is computationally expensive and time-consuming due to the detailed calculations required for each facet. Therefore, existing Monte Carlo-based simulation algorithms for simulating light crossing water-air interfaces [19], [37], [38], [39] typically adopt Cox and Munk's probability density model of surface slopes [35].

Cox and Munk derived a normalized probability distribution formula for the tilt angle γ of the sea surface under certain wind conditions based on data obtained from practical measurements:

$$p(\gamma) = \frac{2}{\sigma^2}\exp\left(-\frac{\tan^2\gamma}{\sigma^2}\right)\tan\gamma\sec^2\gamma \tag{14}$$

where the root mean square surface slope $\sigma = \sqrt{0.003 + 0.00512U}$, and U represents the wind speed over the sea surface in meters per second (m/s). This model effectively simplifies the complex sea surface modeling process, allowing the normal direction of each facet of the sea surface to be directly obtained through statistical rules, thereby significantly enhancing computational efficiency.

IV. EXPERIMENTAL SETUP

Fig. 5a illustrates the schematic diagram of the UWOC measurement link using a 378 nm wavelength LED and NRZ-OOK modulation. Fig. 5b depicts the actual setup, with relevant components labeled accordingly.

At the transmitter end, the near-ultraviolet LED is fixed on the PCB board in airspace near the bottom of the water tank and operates at room temperature. A pseudo-random binary sequence (PRBS) is generated using MATLAB to control the Arbitrary Waveform Generator (AWG) (M9502A) as the digital input signal. The input signal is then amplified using an amplifier (Mini-Circuits ZHL-6A-S+), then attenuated to reduce unnecessary signal intensity using an attenuator (KT3.0-30/1S-2S), and direct current (DC) bias (UTP1310-II-0.3 A) is added to the digital input signal by a Bias-Tee (Mini-Circuits ZFBT-4R2GW-FT+) driving the UV LED.

At the receiver end, an avalanche photodetector (APD410) (Menlo Systems) is mounted at a height of 25cm above the water surface, serving as the optical receiver, with a mixed signal oscilloscope (OSC) (MSO9404A, 4GHz 20 GSa/s) used for ascertain signal presence (link connectivity) and

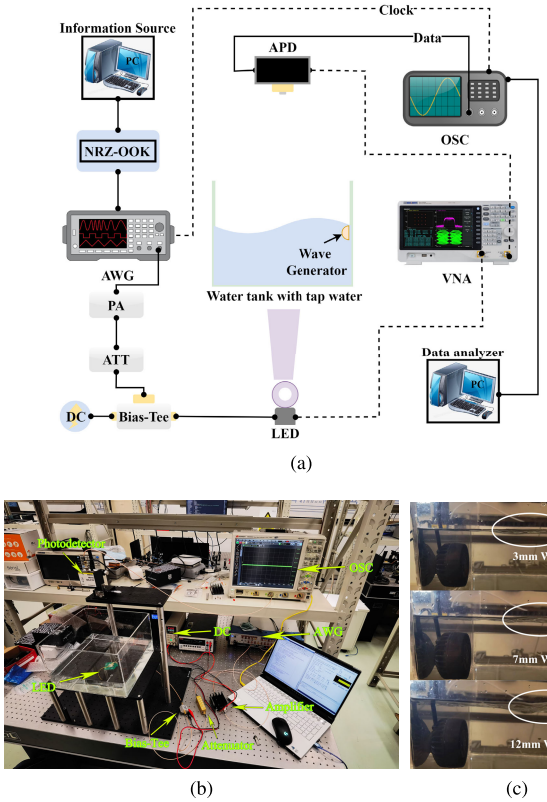

FIGURE 5. (a). Schematic of the experimental setup for LED based across water-air interface uplink optical wireless communications measurements. (b). The actual communication link constructed. (c). Generate waves with average wave amplitudes of 3 mm, 7 mm, and 12 mm using a wave generator.

determine signal magnitude, and MATLAB in personal computer used for eye diagram collection. The vertical distance between the LED and the APD receiver aperture is fixed at 30 cm. Additionally, small signal frequency response measurements are conducted using a Vector Network Analyzer (SVA 1032X) with APD430A2/M. The LED is characterized using an integrating sphere (AIS-2_0.5 m) and optical power meter (LBTEK) for the voltage vs. current and optical power vs. current measurement, and optical power measurements, respectively.

We use a 30 cm × 30 cm × 20 cm quartz water tank. Tap water serves as the water source, with a water depth of 10 cm. As shown in Fig. 5c, a wave generator is positioned close to the water surface to simulate the dynamic undulating characteristics of the water-air interface in a real marine environment, generating waves with average amplitude of 3 mm, 7 mm, and 12 mm (a in (13)), respectively. The wave amplitude is set relatively low to avoid the generation of bubbles, which could potentially interfere with the experiment.

V. EXPERIMENTAL RESULTS AND DISCUSSION

A. TRANSMITTER PERFORMANCE ANALYSIS

We employed an ultraviolet LED light source as the optical transmitter and initially measured its voltage and

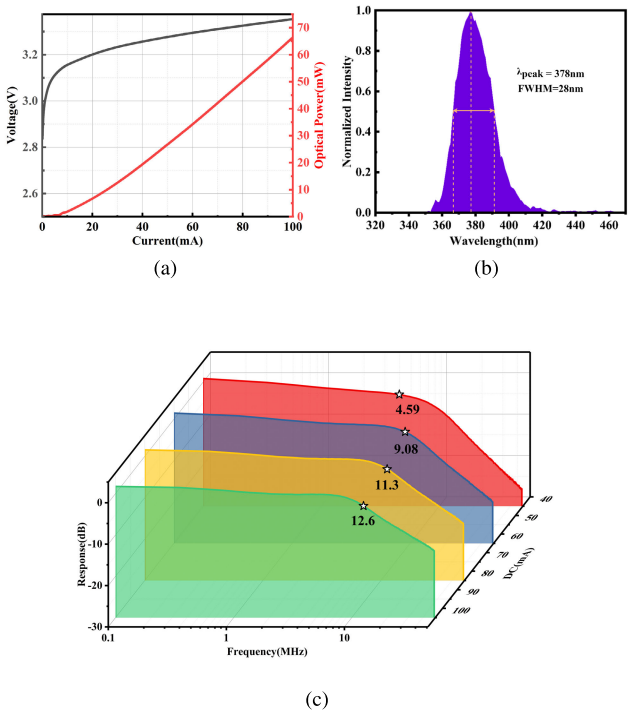

FIGURE 6. (a). Voltage vs. current and optical power vs. current characteristics of the LED with free space. (b). Normalized intensity vs. wavelength of the LED. (c). Frequency response of the system at different bias currents. The −3 dB bandwidth of UWOC links can be predicted to be approximately 13-14 MHz.

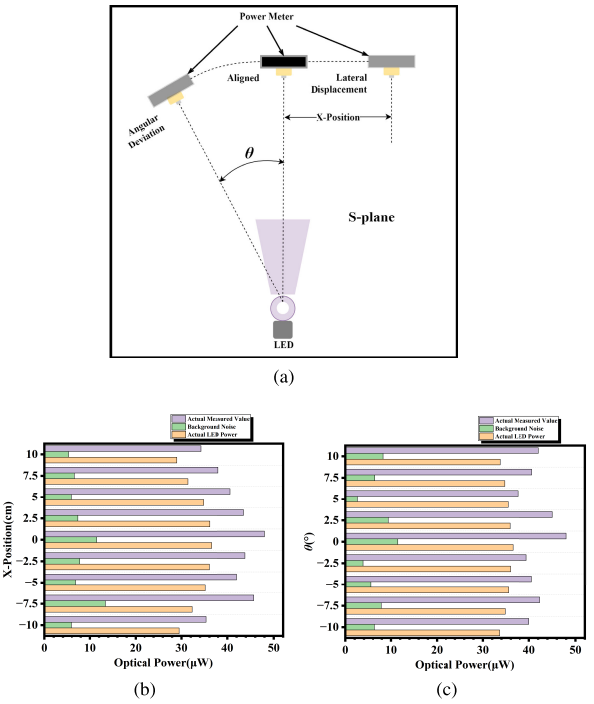

FIGURE 7. (a). Alterations in the X-position and θ were made to measure the optical power of the LED at various lateral displacement and angular deviation positions. (b). The optical power distribution of X-position. (c). The optical power distribution of θ.

optical power variations with current in free space using an integrating sphere (AIS-2_0.5 m). The light-current-voltage (L-I-V) characteristics of the LED are depicted in Fig. 6a. The horizontal axis represents the operating current, the left vertical axis represents the operating voltage, and the right vertical axis represents the optical power. Unlike Laser Diodes (LDs), the LED we used lacks a resonant cavity and are threshold-free devices; their emission is confined to spontaneous emission processes, hence there is no threshold current. At a forward current of 70 mA, the optical output power of the LED in free space is 42 mW. When the signal is modulated by direct current, it causes variations in the LED's optical power, hence the linearity of the L-I curve is crucial [24]. As observed in Fig. 6a (red line), there is a good linear relationship between optical power and current in free space when the current is greater than 40mA, indicating this LED can serve as ideal optical transmitters.

The spectral characteristics of the LED were measured using the integrating sphere, as depicted in Fig. 6b. The horizontal axis represents the wavelength, while the vertical axis represents the normalized light intensity at the corresponding wavelength. The peak wavelength of the spectrum is ∼378 nm, with a full-width at half-maximum (FWHM) of ∼28 nm. It is evident that the LED exhibits negligible light intensity components outside the range of 350 nm to 420 nm.

The frequency response of the link under a 30 cm air-water channel with different bias currents was measured using the network analyzer (SVA 1032X), as shown in Fig. 6c. The X-axis represents frequency, the Y-axis represents bias current, and the Z-axis represents frequency response. As the bias current increases from 45 mA to 105 mA, the system's −3 dB bandwidth expands from 4.59 MHz to 12.6 MHz, exhibiting a decelerating growth trend (it can be predicted that the maximum bandwidth of this 378 nm LED is limited to 13-14 MHz), and the frequency response of the air-water link rapidly declines after the −3dB bandwidth frequency.

B. OPTICAL POWER CHARACTERISTICS

In order to explore the optical power distribution characteristics of the LED in free space, after removing the obstruction between the LED and the optical power meter (primarily the water tank), power measurements were conducted at different positions using the optical power meter, as shown in Fig. 7a:

- Keeping the horizontal height constant (30 cm), lateral displacement distances were varied to position the optical power meter at 0 cm, ±2.5 cm, ±5 cm, ±7.5 cm, and ±10 cm from the center (X-position = 0 cm, ±2.5 cm, ±5 cm, ±7.5 cm, and ±10 cm), with the optical power meter always oriented vertically downward.
- Maintaining a constant distance (30 cm) between the optical power meter and the LED, the angular offset was altered to position the optical power meter at 0°, ±2.5°, ±5°, ±7.5°, and ±10° off the vertical axis (θ = 0°, ±2.5°, ±5°, ±7.5°, and ±10°), with the optical power meter consistently directed towards the LED (equivalent to the optical power meter rotating on a spherical surface

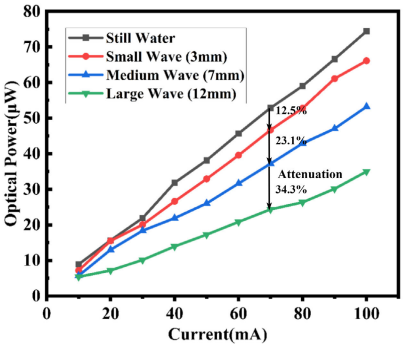

FIGURE 8. The curve of optical power variation with bias current in the actual channel under different wave amplitudes in the aligned transmission state.

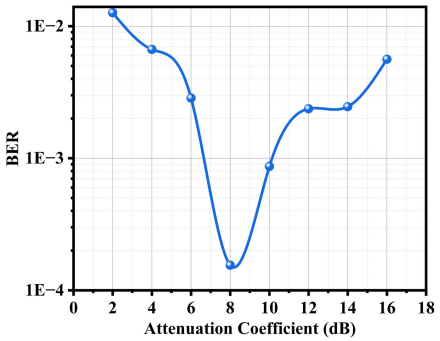

FIGURE 9. The relationship between the attenuation coefficient and the BER under conditions of still water, Rx and Tx alignment, and a data rate of 20 Mbit/s. In this channel scenario, the optimal attenuation coefficient is 8 dB.

and continuously pointing towards the center of the sphere, where the LED is located).

In all the aforementioned measurements, the optical power meter's positions were aligned with the LED on the same plane, denoted as the S-plane.

Five measurements were taken at each position, and the average results are shown in Fig. 7b, 7c. The X-axis represents the received optical power, while the Y-axis of Fig. 7b and Fig. 7c represents the lateral displacement distance and angular deviation from the vertical axis, respectively. The background noise represents the optical power measured when the LED is off. Subtracting the background noise from the actual measured values yields the actual optical power of the LED. It can be observed that the optical power of the LED in free space exhibits characteristics of Gaussian distribution in the S-plane, and the influence of lateral displacement on optical power attenuation is more significant than that of angular deviation.

In our further work, the angular power spectrum density $P(\theta, \phi)$ could be utilized to more accurately model the influence of angular deviations on the distribution of optical power. The spectrum can be formulated as:

$$P(\theta, \phi) = P_0 \exp\left[-\frac{(\theta - \theta_0)^2}{2\sigma_\theta^2}\right] \cdot \exp\left[-\frac{(\phi - \phi_0)^2}{2\sigma_\phi^2}\right] \tag{15}$$

where P_0 is the peak power density, θ_0 and ϕ_0 are the mean angles of arrival, and σ_θ and σ_ϕ represent the standard deviations of the angular spread. Furthermore, this model can also be used for initial estimation of optical power distribution across the air-water interface under dynamic sea surface conditions.

Maintaining a constant distance of 30 cm between the APD receiver aperture and the LED, optical power measurements were conducted under different conditions of wave amplitude (0 mm, 3 mm, 7 mm, 12 mm) in aligned transmission (X-position = 0 cm), as illustrated in Fig. 8. The horizontal axis represents the bias current, while the vertical axis represents the received optical power. Each curve represents the results obtained under a specific wave intensity condition. With increasing wave amplitude, the degree of light refraction by the water surface increases, leading to greater instability in the optical path and consequently an increase in the attenuation of the optical power link, resulting in a decrease in the measured average optical power. For instance, at a bias current of 70 mA, the optical power under static water conditions is 51.8 μW, while under 3 mm wave conditions, it decreases to 45.3 μW, representing a 12.5% attenuation; under 7 mm wave conditions, the optical power decreases to 36.4 μW, representing a 35.6% attenuation; and under 12 mm wave conditions, the optical power decreases to 23.9 μW, representing a 69.9% attenuation. Moreover, increasing the bias current can enhance the chances of photons being captured by the APD, partially compensating for the attenuation.

C. COMMUNICATION PERFORMANCE

To determine the optimal testing point, the bias current was adjusted to a fixed value of 70 mA under still water aligned communication conditions (X-position = 0 cm), with a data rate of 20 Mbit/s. The distance between the APD receiving aperture and the LED was maintained at 30 cm. The attenuation coefficient was gradually adjusted, and the corresponding bit error rate (BER) was recorded, as shown in Fig. 9. When the attenuation coefficient was 2 dB, the BER was 0.57×10^{-2}; as the attenuation coefficient increased to 8 dB, the BER decreased to its minimum point of 0.62×10^{-4}. Continuing to increase the attenuation coefficient to 16 dB, the BER rebounded to 4.39×10^{-3}.

The BER of the received signal is closely related to the dynamic range and of the APD. If the attenuation coefficient of the attenuator is too small, it indicates that the signal is hardly attenuated during the transmission process, leading to excessive signal strength. This may cause the received signal at the receiver to be too strong, exceeding APD's dynamic range. Nonlinear effects, saturation effects, gain noise, and overload effects can cause signal distortion and increased noise, leading to a decrease in the Signal-to-Noise Ratio (SNR), and consequently, an increase in the BER. Conversely, if the attenuation coefficient of the attenuator is

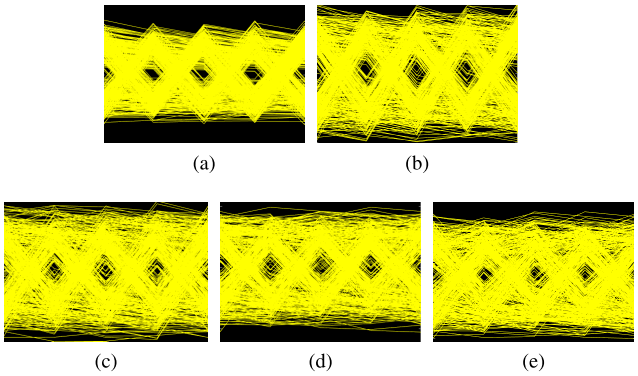

FIGURE 10. Eye diagrams at aligned position for data rates achieved by NRZ-OOK of (a). 30 Mbit/s, (b). 45 Mbit/s, (c). 60 Mbit/s, (d). 62.5 Mbit/s and (e). 75 Mbit/s, respectively.

too large, the signal will be excessively attenuated during the transmission process, resulting in low signal strength. At the receiver, due to insufficient signal strength, the SNR between the signal and noise decreases, which increases the BER. If the signal strength is too low, it may even prevent the receiver from accurately detecting the signal, thus impeding decoding and causing communication failure. In conclusion, selecting an attenuation coefficient of 8 dB ensures optimal channel quality.

To investigate the quality of the received signal and the associated data rates within this channel, we conducted an analysis of the NRZ-OOK modulation scheme. By maintaining the APD at the aligned position (X-position = 0 cm), we gathered eye diagrams and assessed BER across varying data rates. As depicted in Fig. 10, distinct open-eye patterns are observed at 30 Mbit/s, whereas the eye apertures diminish with increasing data rates up to 75 Mbit/s.

Consider the eye diagram opening factor O as:

$$O = \frac{T - \tau_{\mathrm{ISI}}}{T} \tag{16}$$

where T is the bit period and τ_{ISI} is the ISI delay spread. In Fig. 10, as the data transmission rate increases from 30 Mbit/s to 75 Mbit/s, the eye diagram opening factor O significantly decreases while T remains unchanged. This indicates that τ_{ISI} increases, meaning the impact of inter-symbol interference on signal quality progressively increases.

To investigate the impact of deviations in the alignment of the optical transmitter and receiver on communication efficacy, the vertical distance between the APD receiving aperture and the LED was maintained at a fixed 30 cm. The APD receiving aperture was laterally displaced to achieve X-positions of 0 cm, 2.5 cm, and 5 cm, while ensuring that it remained vertically oriented throughout. BERs of the communication channel were measured at different data rates during this process, as illustrated in Fig. 11a. BERs at all three positions gradually increased with rising data rates, reaching the forward error correction (FEC) threshold of 3.8×10^{-3}. The maximum data rates achievable without exceeding the

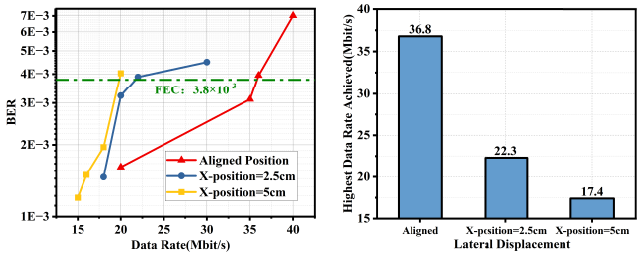

FIGURE 11. (a). Relationship between BER and data rate when X-position = 0 cm, 2.5 cm and 5 cm in still water. (b). The maximum data rates attained when X-position = 0 cm, 2.5 cm and 5 cm where the BER do not exceed the FEC.

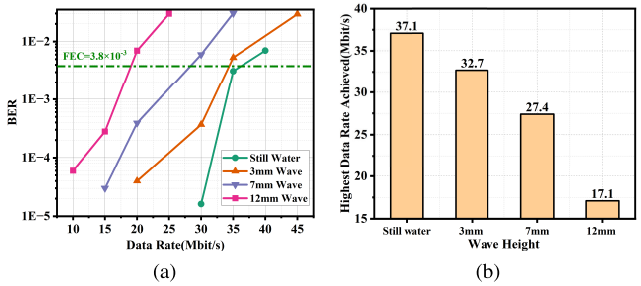

FIGURE 12. (a). Relationship between BER and data rate when the wave amplitude is 3 mm, 7 mm and 12 mm as X-position = 0 cm. (b). The maximum data rates attained when the wave amplitude is 3 mm, 7 mm and 12 mm where the BER do not exceed the FEC.

FEC threshold were recorded for each position, as shown in Fig. 11b.

The results indicate that at X-position = 0 cm, a data transmission rate of 36.8 Mbit/s is achievable, while at X-position = 2.5 cm, an effective data transmission rate of 22.3 Mbit/s can be attained. Even at X-position = 5 cm, a sustained effective data transmission rate of 17.4 Mbit/s is maintained. These findings suggest that precise alignment between transmitter and receiver is not imperative for this configuration. This demonstration underscores a pragmatic and viable approach in cross-medium communication.

To investigate the impact of waves on the performance of NRZ-OOK communication over air-water links, a method was employed where the X-position was fixed at 0 cm while altering the wave amplitude. The approach involved maintaining a constant distance of 30 cm between the APD receiving aperture and the LED, while varying the power of the wave generator to produce stable wave amplitude of 3 mm, 7 mm, and 12 mm. Data rates were adjusted accordingly under different wave amplitude conditions, and the corresponding BERs were recorded, as depicted in Fig. 12a. The maximum data rates where the BER does not exceed the FEC threshold (FEC = 3.8×10^{-3}) were documented for calm water and three wave amplitude scenarios, as illustrated in Fig. 12b.

The results indicate that under constant wave amplitude, an increase in data rate corresponds to a proportional increase in BER. Furthermore, as wave intensity increases, overall communication performance deteriorates, attributed to the

potential introduction of multipath effects by waves, thereby increasing intersymbol interference (ISI) and resulting in channel fading. Additionally, the communication link can sustain an effective transmission rate of 32.7 Mbit/s under low wave conditions, while still maintaining 17.1 Mbit/s under high wave conditions. This suggests that although the channel quality deteriorates in the presence of waves, the communication link still exhibits a degree of robustness, enabling effective communication to a certain extent.

VI. CONCLUSION

In this paper, we investigated the across water-air-interface wireless optical channel in the presence of waves, establishing an UV communication uplink. We investigated the optical power distribution of LED under lateral displacement and angular deviation, as well as the optical power characteristics under varying wave intensities and bias currents. Based on conventional wireless optical line-of-sight transmission modes, an innovative approach utilizing the UV scattering characteristics of a 378 nm LED for non-aligned communication is proposed and its feasibility validated, thus addressing the gap in the 370 nm-400 nm wavelength range within this research domain. Employing NRZ-OOK modulation, data rates of 17.4 Mbit/s under a lateral deviation of 5 cm in the still water condition and 17.1 Mbit/s under aligned link in the presence of 12 mm wave amplitude are achieved, leveraging the scattering properties of UV light. The BER and received optical power indicate that increasing wave amplitude and misalignment between the Tx and Rx both result in channel attenuation in the air-water link, thereby diminishing the communication performance. This study validates the efficacy of UV communication under high-intensity waves, offering a novel approach for direct communication utilizing scattering characteristics without reliance on relays in non-aligned scenarios.

Field trials of the system is in progress, which will integrate blue-green and ultraviolet LED arrays as transmitter. Adaptive loading techniques will be employed to enhance link stability and wave robustness based on spatialtemporal properties of wave.

REFERENCES

[1] C. M. G. Gussen, P. S. R. Diniz, M. L. R. Campos, W. A. Martins, F. M. Costa, and J. N. Gois, "A survey of underwater wireless communication technologies," *J. Commun. Inf. Syst.*, vol. 31, no. 1, pp. 242–255, Oct. 2016, doi: 10.14209/jcis.2016.22.

[2] J. Hu, Z. Guo, J. Shi, X. Jiang, Q. Chen, H. Chen, Z. He, Q. Song, S. Xiao, S. Yu, N. Chi, and C. Shen, "A metasurface-based full-color circular autofocusing airy beam transmitter for stable high-speed underwater wireless optical communications," *Nature Commun.*, vol. 15, no. 1, pp. 29–44, Apr. 2024, doi: 10.1038/s41467-024-47105-x.

[3] H. M. Oubei, C. Shen, A. Kammoun, E. Zedini, K.-H. Park, X. Sun, G. Liu, C. H. Kang, T. K. Ng, M.-S. Alouini, and B. S. Ooi, "Light based underwater wireless communications," *Jpn. J. Appl. Phys.*, vol. 57, no. 8S2, Jul. 2018, Art. no. 08PA06, doi: 10.7567/jjap.57.08pa06.

[4] M. Stojanovic and J. Preisig, "Underwater acoustic communication channels: Propagation models and statistical characterization," *IEEE Commun. Mag.*, vol. 47, no. 1, pp. 84–89, Jan. 2009, doi: 10.1109/MCOM.2009.4752682.

[5] M. Chitre, S. Shahabudeen, L. Freitag, and M. Stojanovic, "Recent advances in underwater acoustic communications & networking," in *Proc. OCEANS*, Sep. 2008, pp. 1–10.

[6] S. Basagni, M. Conti, S. Giordano, and I. Stojmenovic, "Advances in underwater acoustic networking," in *Mobile Ad Hoc Networking: The Cutting Edge Directions*. New York, NY, USA: Wiley, 2013, pp. 804–852.

[7] X. Che, I. Wells, G. Dickers, P. Kear, and X. Gong, "Re-evaluation of RF electromagnetic communication in underwater sensor networks," *IEEE Commun. Mag.*, vol. 48, no. 12, pp. 143–151, Dec. 2010, doi: 10.1109/MCOM.2010.5673085.

[8] Z. Zeng, S. Fu, H. Zhang, Y. Dong, and J. Cheng, "A survey of underwater optical wireless communications," *IEEE Commun. Surveys Tuts.*, vol. 19, no. 1, pp. 204–238, 1st Quart., 2017, doi: 10.1109/COMST.2016.2618841.

[9] D. K. Borah, A. C. Boucouvalas, C. C. Davis, S. Hranilovic, and K. Yiannopoulos, "A review of communication-oriented optical wireless systems," *EURASIP J. Wireless Commun. Netw.*, vol. 2012, no. 1, pp. 1–28, Mar. 2012, doi: 10.1186/1687-1499-2012-91.

[10] Y. Hou, "A tutorial on laser-based visible light communications," *Chin. Opt. Lett.*, vol. 22, pp. 1–9, May 2024.

[11] J. Wang, J. Hu, C. Guan, Y. Hou, Z. Xu, L. Sun, Y. Wang, Y. Zhou, B. S. Ooi, J. Shi, Z. Li, J. Zhang, N. Chi, S. Yu, and C. Shen, "High-speed GaN-based laser diode with modulation bandwidth exceeding 5 GHz for 20 gbps visible light communication," *Photon. Res.*, vol. 12, no. 6, p. 1186, 2024, doi: 10.1364/prj.516829.

[12] S. Zhu, X. Chen, X. Liu, G. Zhang, and P. Tian, "Recent progress in and perspectives of underwater wireless optical communication," *Prog. Quantum Electron.*, vol. 73, Sep. 2020, Art. no. 100274, doi: 10.1016/j.pquantelec.2020.100274.

[13] H. M. Oubei, E. Zedini, R. T. ElAfandy, A. Kammoun, M. Abdallah, T. K. Ng, M. Hamdi, M.-S. Alouini, and B. S. Ooi, "Simple statistical channel model for weak temperature-induced turbulence in underwater wireless optical communication systems," *Opt. Lett.*, vol. 42, no. 13, p. 2455, Jul. 2017, doi: 10.1364/ol.42.002455.

[14] E. Zedini, H. M. Oubei, A. Kammoun, M. Hamdi, B. S. Ooi, and M.-S. Alouini, "Unified statistical channel model for turbulence-induced fading in underwater wireless optical communication systems," *IEEE Trans. Commun.*, vol. 67, no. 4, pp. 2893–2907, Apr. 2019, doi: 10.1109/TCOMM.2019.2891542.

[15] S. Arnon, "Underwater optical wireless communication network," *Opt. Eng.*, vol. 49, no. 1, Jan. 2010, Art. no. 015001, doi: 10.1117/1.3280288.

[16] L. J. Johnson, F. Jasman, R. J. Green, and M. S. Leeson, "Recent advances in underwater optical wireless communications," *Underwater Technol., Int. J. Soc. Underwater*, vol. 32, no. 3, pp. 167–175, Nov. 2014, doi: 10.3723/ut.32.167.

[17] X. Sun, M. Kong, C. Shen, C. H. Kang, T. K. Ng, and B. S. Ooi, "On the realization of across wavy water-air-interface diffuse-line-of-sight communication based on an ultraviolet emitter," *Opt. Exp.*, vol. 27, no. 14, p. 19635, Jul. 2019, doi: 10.1364/oe.27.019635.

[18] X. Sun, Z. Zhang, A. Chaaban, T. K. Ng, C. Shen, R. Chen, J. Yan, H. Sun, X. Li, J. Wang, J. Li, M.-S. Alouini, and B. S. Ooi, "71-Mbit/s ultraviolet-B LED communication link based on 8-QAM-OFDM modulation," *Opt. Exp.*, vol. 25, no. 19, p. 23267, Sep. 2017, doi: 10.1364/oe.25.023267.

[19] J. Qin, M. Fu, and B. Zheng, "Analysis of wavy surface effects on the characteristics of wireless optical communication downlinks," *Opt. Commun.*, vol. 507, Mar. 2022, Art. no. 127623, doi: 10.1016/j.optcom.2021.127623.

[20] X. Sun, M. Kong, O. Alkhazragi, C. Shen, E.-N. Ooi, X. Zhang, U. Buttner, T. K. Ng, and B. S. Ooi, "Non-line-of-sight methodology for high-speed wireless optical communication in highly turbid water," *Opt. Commun.*, vol. 461, Apr. 2020, Art. no. 125264, doi: 10.1016/j.optcom.2020.125264.

[21] T. Cao, X. Gao, T. Wu, C. Pan, and J. Song, "Single-scatter path loss model of LED-based non-line-of-sight ultraviolet communications," *Opt. Lett.*, vol. 46, no. 16, p. 4013, Aug. 2021, doi: 10.1364/ol.435418.

[22] M. Sait, X. Sun, O. Alkhazragi, N. Alfaraj, M. Kong, T. Khee Ng, and B. S. Ooi, "The effect of turbulence on NLOS underwater wireless optical communication channels [invited]," *Chin. Opt. Lett.*, vol. 17, no. 10, May 2019, Art. no. 100013, doi: 10.3788/col201917.100013.

[23] C. Yu, X. Chen, Z. Zhang, G. Song, J. Lin, and J. Xu, "Experimental verification of diffused laser beam-based optical wireless communication through air and water channels," *Opt. Commun.*, vol. 495, Sep. 2021, Art. no. 127079, doi: 10.1016/j.optcom.2021.127079.

[24] Z. Lv, G. He, C. Qiu, and Z. Liu, "Investigation of underwater wireless optical communications links with surface currents and tides for oceanic signal transmission," *IEEE Photon. J.*, vol. 13, no. 3, p. 18, Jun. 2021, doi: 10.1109/JPHOT.2021.3076895.

[25] Y. Chen, M. Kong, T. Ali, J. Wang, R. Sarwar, J. Han, C. Guo, B. Sun, N. Deng, and J. Xu, "26 m/55 gbps air-water optical wireless communication based on an OFDM-modulated 520-nm laser diode," *Opt. Exp.*, vol. 25, no. 13, p. 14760, Jun. 2017, doi: 10.1364/oe.25.014760.
[26] H. Kaushal and G. Kaddoum, "Underwater optical wireless communication," *IEEE Access*, vol. 4, pp. 1518–1547, 2016, doi: 10.1109/ACCESS.2016.2552538.
[27] D. Han, Y. Liu, K. Zhang, P. Luo, and M. Zhang, "Theoretical and experimental research on diversity reception technology in NLOS UV communication system," *Opt. Exp.*, vol. 20, no. 14, p. 15833, Jul. 2012, doi: 10.1364/oe.20.015833.
[28] R. Sahoo and P. Shanmugam, "Effect of the complex air–sea interface on a hybrid atmosphere-underwater optical wireless communications system," *Opt. Commun.*, vol. 510, May 2022, Art. no. 127941, doi: 10.1016/j.optcom.2022.127941.
[29] Y. Hou, Z. Wang, M. Liu, S. Yi, X. Wang, L. Xia, G. Liu, J. Shi, Z. Li, J. Zhang, N. Chi, and C. Shen, "Wide field-of-view laser-based white light transmitter for visible light communications," *Opt. Lett.*, vol. 49, no. 10, p. 2805, May 2024.
[30] Y. Shao, Y. Di, and L.-K. Chen, "Adaptive loading for water-air SIMO OWC system based on the temporal and spatial properties of waves," in *Proc. Opt. Fiber Commun. Conf. Exhib. (OFC)*, San Francisco, CA, USA, Jun. 2021, pp. 1–3.
[31] D. Anguita, D. Brizzolara, G. Parodi, and Q. Hu, "Optical wireless underwater communication for AUV: Preliminary simulation and experimental results," in *Proc. OCEANS IEEE Spain*, Santander, Spain, Jun. 2011, pp. 1–5, doi: 10.1109/Oceans-Spain.2011.6003598.
[32] C. D. Mobley, B. Gentili, H. R. Gordon, Z. Jin, G. W. Kattawar, A. Morel, P. Reinersman, K. Stamnes, and R. H. Stavn, "Comparison of numerical models for computing underwater light fields," *Appl. Opt.*, vol. 32, no. 36, p. 7484, 1993, doi: 10.1364/ao.32.007484.
[33] Y. Zhang, Y. Wang, and A. Huang, "Influence of suspended particles based on Mie theory on underwater laser transmission," *Chin. J. Lasers*, vol. 45, no. 5, May 2018, Art. no. 0505002, doi: 10.3788/cjl201845.0505002.
[34] D. Toublanc, "Henyey–Greenstein and Mie phase functions in Monte Carlo radiative transfer computations," *Appl. Opt.*, vol. 35, no. 18, p. 3270, 1996, doi: 10.1364/ao.35.003270.
[35] C. Cox and W. Munk, "Statistics of the sea surface derived from sun glitter," *J. Mar. Res.*, vol. 13, pp. 198–227, Jan. 1954.
[36] J. Ke, "Research on visible light transmission characteristics of LED in seawater-atmosphere cross medium environment," M.S. thesis, Electron. Inf., Xi'an Univ. Technol., Xi'an, Shaanxi, China, 2023.
[37] B. Rao Angara, P. Shanmugam, and H. Ramachandran, "Influence of sea surface waves and bubbles on the performance of underwater-to-air optical wireless communication system," *Opt. Laser Technol.*, vol. 174, Jul. 2024, Art. no. 110652, doi: 10.1016/j.optlastec.2024.110652.
[38] T. Lin, C. Gong, J. Luo, and Z. Xu, "Dynamic optical wireless communication channel characterization through air-water interface," in *Proc. IEEE/CIC Int. Conf. Commun. China (ICCC Workshops)*, Chongqing, China, Aug. 2020, pp. 173–178, doi: 10.1109/ICCCWorkshops49972.2020.9209928.
[39] T. Lin, C. Fu, T. Wei, N. Huang, X. Liu, L. Tang, L. Su, J. Luo, and C. Gong, "Waving effect characterization for water-to-air optical wireless communication," *J. Lightw. Technol.*, vol. 41, no. 1, pp. 120–136, Jan. 2023, doi: 10.1109/JLT.2022.3213339.

CHENYU GUO was born in Xi'an, Shannxi, China. He is currently pursuing the degree with the Department of Communication Science and Engineering (CSE), School of Information Science and Technoloigy (SIST), Fudan University. His research interests include wireless optical communication, semiconductor heterostructure epitaxial growth technology, and the field of digital watermarking attack and defense.

ZENGXIN LI received the B.E. degree in communication engineering from Fudan University, Shanghai, China, in 2023, where she is currently pursuing the master's degree.

She is a member of the Department of Communication Science and Engineering, Key Laboratory for Information Science of Electromagnetic Waves (MoE), Shanghai Engineering Research Center of Low-Earth-Orbit Satellite Communication and Applications, Fudan University. Her research interests include optical wireless communication, MIMO, and underwater optical communication.

LULU ZHA was born in Yangzhou, Jiangsu, China. She is currently pursuing the degree with the Department of Electronic Information, School of Information Science and Technology (SIST), Fudan University. Her research interests include wireless optical communication, micro-LED arrays, and high-speed laser communication.

ZHICHONG WANG received the B.E. degree in communication engineering from Donghua University, Shanghai, China. He is currently pursuing the M.E. degree with Fudan University, Shanghai. His research interests include visible light communication and laser lighting.

HAOLIN JIA (Graduate Student Member, IEEE) received the B.A. degree in physics from Nanchang University, in 2021, and the M.S. degree in materials science and engineering from the University of Science and Technology of China, in 2024. He is currently pursuing the degree with Fudan University. His research project is visible light communication.

YUQI HOU received the bachelor's degree from the School of Information Science. She is currently pursuing the master's degree in communication and information system with Fudan University. Her current research interests include visible light communication systems, particularly the implementation of wide-field-of-view visible light communication systems.

JIANYANG SHI (Member, IEEE) received the Ph.D. degree in electromagnetic field and microwave technology from Fudan University, China, in 2019. He was a Senior Engineer with Huawei's Shanghai Research Institute and a Postdoctoral Fellow with Fudan University. He is currently an Associate Research Fellow with Fudan University. His current research interests include optical communications, optical wireless communications, digital signal processing, visible light communications, and fiber communications. He was a recipient of the IEEE Photonics Society Graduate Student Fellowship. He was the Editorial Board Member of *Photonics*.

ZIWEI LI received the Ph.D. degree from the Department of Automation, Tsinghua University. She is currently an Associate Researcher with the School of Information Science and Technology, Fudan University, China. Her research interests include the study of computational imaging, advanced microscopy, and intelligent optical communication and sensing.

JUNWEN ZHANG received the Ph.D. degree from Fudan University, in 2014. From 2012 to 2015, he studied and worked with Georgia Tech. He joined ZTE (Tx), in 2016, working on next-gen high-speed optical access networks. He has published more than 180 articles on high-speed optical transmission, access, and signal processing. He received the Marconi Society Paul Baran Young Scholar Award, in 2016, and the IEEE Photonics Society Graduate Student Fellowship and Wang Daheng Optics Award, in 2013.

NAN CHI (Senior Member, IEEE) received the B.S. and Ph.D. degrees in electrical engineering from Beijing University of Posts and Telecommunications, Beijing, China, in 1996 and 2001, respectively. From July 2001 to December 2004, she was an Assistant Professor with the Research Center COM, Technical University of Denmark, Lyngby, Denmark. From January 2005 to April 2006, she was a Research Associate with the University of Bristol, Bristol, U.K. In June 2006, she joined Wuhan National Laboratory for Optoelectronics, Huazhong University of Science and Technology, where she was a Full Professor. In June 2008, she was with the School of Information Science and Engineering, Fudan University. She is the author or co-author of more than 200 articles. She has been the Chair of the APOC 2007 OsRT Workshop and ACP 2010. Her research interests include coherent optical transmission, visible light communication, and optical packet/burst switching. She was a Technical Program Committee Member of many conferences, such as APOC 08, ICAIT09, ACP 2011, WOCC 2012, ACP 2013, and IWOO 2014. She was a recipient of the New Century Excellent Talents Awards from the Education Ministry of China, Shanghai Shu Guang Scholarship, Japanese OKAWA Intelligence Fund Award, Pujiang Talent of Shanghai City, and Ten Outstanding IT Young Persons Awards of Shanghai City.

CHAO SHEN (Senior Member, IEEE) received the B.Sc. degree in materials physics from Fudan University and the Ph.D. degree in electrical engineering from KAUST. He is currently a Professor with the School of Information Science and Technology, Fudan University. He has published more than 100 peer-reviewed publications in the fields of III-Nitride optoelectronics devices, semiconductor lasers, superluminescent diodes, photonics integrated circuit, visible light communications (VLC), and underwater wireless optical communications (UWOC). He has served as a TPC Member and an Invited Speaker at many IEEE, Optica, and SPIE conferences. He is a recipient of the 2022 Okawa Foundation Research Grant. He has served as an Associated Editor of IEEE Photonics Journal.